Electronic Supplementary Material (ESI) for Nanoscale Horizons.


# Supplementary Information

for

# All-optical manipulation of singlet exciton transport in individual supramolecular nanostructures by triplet gating

Bernd Wittmann[1], Till Biskup[2], Klaus Kreger[3,4], Jürgen Köhler[1,4,5], Hans-Werner Schmidt[3,4], Richard Hildner*[1,6]

**Affiliations:**

[1]Spectroscopy of Soft Matter, University of Bayreuth, Universitätsstraße 30, 95447 Bayreuth, Germany.

[2]Institute of Physical Chemistry, University of Freiburg, Albertstraße 21, 79104 Freiburg, Germany
Current address: Chair of Physical Chemistry and Chemical Education, University of Saarland, Campus B2 2, 66123 Saarbrücken, Germany.

[3]Macromolecular Chemistry I, University of Bayreuth, Universitätsstraße 30, 95447 Bayreuth, Germany.
[4]Bavarian Polymer Institute, Universitätsstraße 30, 94557 Bayreuth, Germany

[5]Bayreuth Institute of Macromolecular Research (BIMF), University of Bayreuth, Universitätsstraße 30, 94557 Bayreuth, Germany

[6]Zernike Institute for Advanced Materials, University of Groningen, Nijenborgh 4, 9747 AG Groningen, The Netherlands.

*Correspondence to: r.m.hildner@rug.nl.

# Contents:

## 1. Materials and Methods

***Materials and sample preparation.***

The synthesis, purification and characterization of the supramolecular CBT building block are described in detail elsewhere [1].

*Molecularly dissolved solution of CBT.* A 40 µM solution in THF (boiling point: 66 °C) was refluxed for 20 minutes under stirring and was then allowed to cool to room temperature.

*Self-assembly of CBT into bundles of supramolecular nanofibres.* CBT was added to anisole (boiling point: 154 °C) at a concentration of 40 µM (~100 p.p.m., 0.01 wt%) or 400 µM (~1000 p.p.m., 0.1 wt%). A homogeneous dispersion was ensured by ultrasonication for 15 minutes. The dispersions were refluxed for 30 minutes under stirring and were then allowed to cool to room temperature. All solvents were of HPLC grade and used as received [2].

*Motivation for the choice of the bundled nanofibers*. For this work we use bundles of supramolecular nanofibers that comprise more than 1000 nanofibres and thus provide a sufficiently high signal-to-noise and signal-to-background ratio. Isolated, single nanofibers, as we reported in Ref.[2], feature only a weak fluorescence signal due to their nearly ideal H-type nature with only weakly optically allowed emissive transitions of singlet excitons to the singlet ground state. Moreover, in single nanofibres reported in our previous work[2,3] we observed exciton trapping in (very) low-lying exciton states[3]. Therefore, the resulting spatio-temporal data (such as in Fig. 3 in the main text) in the absence of the triplet-laser can be strongly biased to one direction even without a local triplet population. This effect is avoided by averaging over the many nanofibers in a bundled system. Moreover, for the specific system in ref. 4, the observation of long-range transport along the core of the nanofibres was only indirect via the photoluminescence of peripheral groups that are populated after long-range transport along the nanofibre's core by an incoherent Forster-transfer step from the fibre's core to the periphery. This Forster-transfer step will obscure precise temporal information on the singlet exciton dynamics within the nanofibres' core, which is, however, required for the analysis done in this present work.

***Methods.***

*Time-resolved detection of the electron paramagnetic resonance (TREPR).* TREPR spectroscopy with a time resolution of down to 10 ns allows for real-time observation, e.g., of short-lived radical-pair and triplet states generated by pulsed laser excitation [4]. In contrast to conventional continuous-wave EPR spectroscopy, which usually involves magnetic-field modulation to improve the signal-to-noise ratio, TREPR is recorded in a high-bandwidth direct-detection mode, so as not to constrain the time resolution of the experiment. Consequently, positive and negative signal amplitudes in TREPR correspond to enhanced absorptive (A) and emissive (E) electron-spin polarisations of the EPR transitions, respectively. TREPR experiments were performed at 80 K using a commercial EPR spectrometer (Bruker ESP380E, Bruker EMX) in conjunction with a Bruker microwave bridge (ER 046 MRT, EMX premiumX). The sample was placed in a synthetic-quartz (Suprasil) sample tube (3 mm inner diameter) and irradiated in a dielectric-ring resonator (Bruker ER 4118X-MD5), which was immersed in a helium gas-flow cryostat (Oxford CF-935) cooled with liquid nitrogen or a closed-cycle cryostat (Cryogenic CF VTC) cooled with helium. The temperature was regulated to ±0.1 K by a temperature controller (Oxford ITC-503, Lake Shore 350). The time resolution of the experimental setup was in the 10 ns range (Bruker ESP380E) and 100 ns range (Bruker EMX). A microwave frequency counter (Hewlett-Packard HP 5352B, Bruker EMX) was used to monitor the microwave frequency. Optical excitation at the respective wavelengths was carried out with an optical parametric oscillator (OPO) system (Opta BBO-355-vis/IR, GWU primoScan/BB/120-INDI) pumped by an Nd:YAG laser (Spectra Physics, Quanta Ray GCR 190-10, Quanta-Ray INDI PS 51/52) with a pulse width of approximately 6 ns, and a pulse energy of 1 mJ. The repetition rate of the laser was set to 10/20 Hz. A transient recorder (LeCroy 9354A, LeCroy HDO9204) with a digitizing rate of 2 ns/11 bit, 4 ns/8 bit was used to acquire the time-dependent EPR signal. To eliminate the background signal induced by the laser entering the EPR cavity, TREPR signals were accumulated at off-resonance magnetic-field positions (background) and subtracted from those recorded on-resonance. This background signal is completely independent in its shape from both, laser wavelength and magnetic field, and normally long-lived compared to the detected spin-polarised EPR signal. Further experimental parameters: Microwave frequency, 9.69010 GHz, microwave power: 2 mW (20 dB attenuation, source power 200 mW), Bruker ESP: frequency-mixer detection, video amplifier set to 42 dB amplification and 25 MHz

bandwidth, 1000 averages per point, Bruker EMX: diode detection, 100 averages per point, laser excitation at 464 nm with 1 mJ per pulse and a shot repetition rate of 10/20 Hz.

*Optical experiments.* Time-resolved photoluminescence decays of dispersions (in cuvettes) were recorded with a confocal fluorescence microscope (MicroTime 200, Picoquant), equipped with a 405 nm pulsed diode laser (LDH-D-C-405, Picoquant) at a repetition rate of 0.2 MHz with an air objective (NA=0.4). The excitation fluence was $4.3 \cdot 10^{16}$ photons/(pulse·cm²). In detection, we used a long-pass filter LP561 (AHF Analysentechnik).

Fluence- and repetition rate dependent time-resolved fluorescence decays of dispersions (in cuvettes) were recorded with a home-built microscope (see below), equipped with a 450 nm pulsed laser diode (LDH-P-C-450B, Picoquant) and an air objective (NA=0.5). An additional long-pass filter LP545 (AHF Analysentechnik) was used to suppress the CBT monomer emission in the dispersion. All measurements on dispersions were conducted using Hellma QS quartz-glass cuvettes.

Optical imaging and spectroscopy of single bundles of supramolecular nanofibres. The 40 µM-dispersion of bundles in anisole was spin-coated on microscopy coverslips (borosilicate glass; thickness 0.17 µm; Carl Roth). All samples were dried under vacuum. Optical imaging and spectroscopy were performed using a home-built microscope (see Ref. [2]). The excitation sources were pulsed diode lasers (LDH-P-C-450B, LDH-D-C-420, Picoquant; 70 ps pulse duration) that operate at a wavelength of 450 nm and 420 nm, respectively. Note that the different wavelengths of our laser excitations have no effect on the concept presented here as long as those resonantly excite singlet excitons (see the absorption spectrum in Fig. S2). The temporal separation between the pulses from both lasers is controlled by two laser drivers (PDL-800-D, PDL800-B, Picoquant), which are connected via their respective Sync-output and Sync-input and thus both lasers use the same internal clock. Due to the cable length and the internal delay of the external trigger input of the laser driver, the 450 nm laser is delayed by 120 ns with respect to the 420 nm laser. A shutter in front of each laser allows for a separate activation of the lasers. The spatial separation of the lasers in the sample plane is achieved by two excitation paths. In one of the paths, we implemented a tilting mirror to scan the 420 nm laser. The lasers were combined via a 50/50 beam splitter and directed to the microscope, which was equipped with an

infinity-corrected, high-numerical aperture, oil-immersion objective (PlanApo, 60×, numerical aperture 1.45; Olympus). The sample was placed in the focal plane of the objective, and the sample position was controlled by a piezo-stage (Tritor 102 SG, from piezosystem jena). Photoluminescence was collected by the same objective and passed a set of dielectric filters (dichroic beam splitter z460RDC, long-pass filter LP467; AHF Analysentechnik) to suppress scattered or reflected laser light.

The detection beam path is equipped with a closed-loop piezo scan mirror (S-335.2.SH, PI) and a single-photon-counting avalanche photodiode (MPD, Picoquant) to position the detection spot independently of the confocal excitation spot. The electrical signal of the photodiode was fed into a time-correlated single-photon-counting module (TimeHarp 260 PICO, Picoquant).

In imaging mode, the photoluminescence signal was imaged onto a CMOS camera (Zyla 4.2 sCMOS, Andor). In this mode, we used two illumination methods. First, for widefield illumination, we flipped an additional lens (widefield lens) into the excitation beam path to focus the laser light into the back-focal plane of the microscope objective. This allows for nearly uniform illumination of a large area with ~70 µm diameter in the sample plane, to acquire overview PL images of our samples and to identify elongated nanostructures (Fig. 3a, see also the AFM image in Fig. S1). Second, for confocal illumination, the widefield lens was removed and the laser light was tightly focused to a spot with a full width at half maximum (FWHM) of ~211 nm for the 450 nm laser in the sample plane and 265 nm for the 420 nm laser, respectively (see Fig. S10). A flip-mirror allows to switch between imaging and single-photon counting mode of the setup.

For measurements on isolated bundles of supramolecular nanofibres, we used a repetition rate of 5 MHz and an excitation intensity of 115 W $cm^{-2}$ for confocal illumination of the 450nm laser, respectively, 540 W $cm^{-2}$ for the 420nm laser. For widefield illumination, we used an excitation intensity of 1 W $cm^{-2}$. All experiments were carried out at room temperature under ambient conditions.

For the TCSPC-data in Figs. 2b and S2b we integrated for 20 minutes, and for the decay curves in Figs. 2c and S3 we integrated until the first time bin reaches 5000 counts. To avoid pile-up we ensured that the detection count rate was less than 1% of the laser repetition rate by using a continuously variable metallic neutral density filter in front of the detector. The instrument response function (see Fig. S3) was measured

using a strongly quenched aqueous solution of fluorescein (quenched with potassium iodide) at very low detection count rates ($\ll 1\%$ of the laser repetition rate). Since the PL-decay curves do not behave mono-exponentially, all lifetimes reported correspond to amplitude-weighted average lifetimes (see Fig. S3).

To quantitatively analyse the energy transport, we calculated the second moments $\mu_2(t)$ (a measure for the widths) at time $t$ of our spatial intensity distributions $I(x,t)$ in accordance with our previous publication [2]. The second moment at each point in time is defined as

$$\mu_2 = \frac{1}{N} \int (x-\mu_1)^2 I(x,t_i)dx,$$

where $N = \int I(x,t)dx$ is the integrated fluorescence intensity and $\mu_1(t) = \frac{1}{N} \int xI(x,t)dx$ is the corresponding first moment (measure for the centre of mass of the profile). We evaluate changes of the second moments $\mu_2(t)$ with respect to the second moment of the initial distributions $\mu_2(t=0)$ as a measure for singlet exciton diffusion, i.e.,

$$\Delta\mu_2(t) = \mu_2(t=0) - \mu_2(t).$$

To evaluate the changed singlet exciton transport lengths (e.g. Fig. 3f), we fitted a power law to the extracted $\Delta\mu_2(t)$ curves, i.e., $\Delta\mu_2 = At^{\alpha}$, in the presence and absence of the triplet population, which describes the transport dynamics to a good approximation for times $t > 1\,ns$. We evaluated the singlet exciton diffusion lengths $L_D = \sqrt{\Delta\mu_2(t)}$ from our fit at time $t = 5\,ns$. Then, we calculated the difference between the diffusion lengths from our reference experiment $L_D^{Ref}$ and the experiment with both lasers active, i.e., $\Delta L_D = L_D^{Ref} - L_D$. The histogram in Fig. 3g shows those measurements with a successful manipulation of the singlet excitons, i.e., where the calculated difference in diffusion length is greater than the corresponding error.

*Simulations*. Simulations of triplet spectra have been performed using the fitting framework TSim [5] based on the EasySpin software package [6] available for MATLAB® (MathWorks), and here the routine “pepper”. Parameters included were the g and D tensor and the triplet sublevel populations (in zero field). Line broadening ($\Gamma$) was included using a combination of Lorentzian ($\Gamma_L$) and Gaussian ($\Gamma_G$) lines. For all

simulations, the $g$ tensor was assumed to be isotropic, with $g_{iso} = 2.002$. This left the parameters $D$ and $E$ of the zero-field splitting tensor $D$, the populations $p_1$, $p_2$, and $p_3$, and the two line widths $\Gamma_L$ and $\Gamma_G$ as the only free parameters that were adjusted. For a more detailed explanation of these parameters and their meanings, see Ref. [4].

Fitting the spectral simulations to the experimental data was done with the routine "lsqcurvefit" from the MATLAB® Optimization Toolbox™ using the trust-region-reflective least squares algorithm. For the final simulation parameters obtained from fitting, cf. Table S1. For the bundles, no simulation consisting of a single triplet species could be successfully fitted to the data, pointing to multiple concurrent triplet species present in the bundles.

For the numerical simulation of the spatio-temporal singlet-triplet annihilation shown in Figs. S5 and S6, we used home-written Python-scripts. Further details are outlined below in the supplementary information, section 2.

**Table S1. Simulation parameters for the TREPR spectrum** shown in Fig. S2. The simulation parameters are the complete set of parameters used for simulating the spectrum shown in Fig. S2. $\Gamma$ is the line width the simulation has been convoluted with.

| $g_{iso}$ | $p_1$ | $p_2$ | $p_3$ | $D$ / MHz | $E$ / MHz | $\Gamma_G$ / mT | $\Gamma_L$ / mT |
|---|---|---|---|---|---|---|---|
| 2.002 | 0.289 | 0.339 | 0.372 | 1008±2 | 187±2 | 4.9±0.6 | 4.6±0.4 |

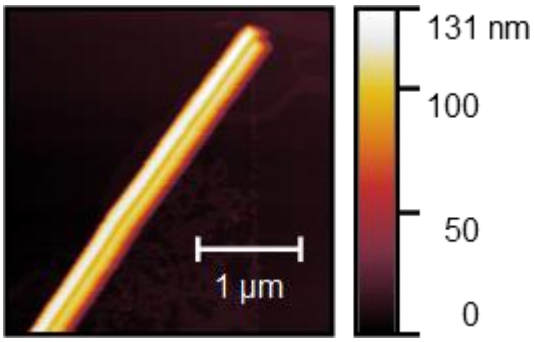


**Fig. S1: AFM image of a bundle of nanofibres.** The sample was spin-coated from a 40 µM dispersion of s-CBT in anisole. The bundle consists of two thinner bundles with widths and heights in the order of 100 nm and lengths of several micrometres (cf. Ref. [2]).

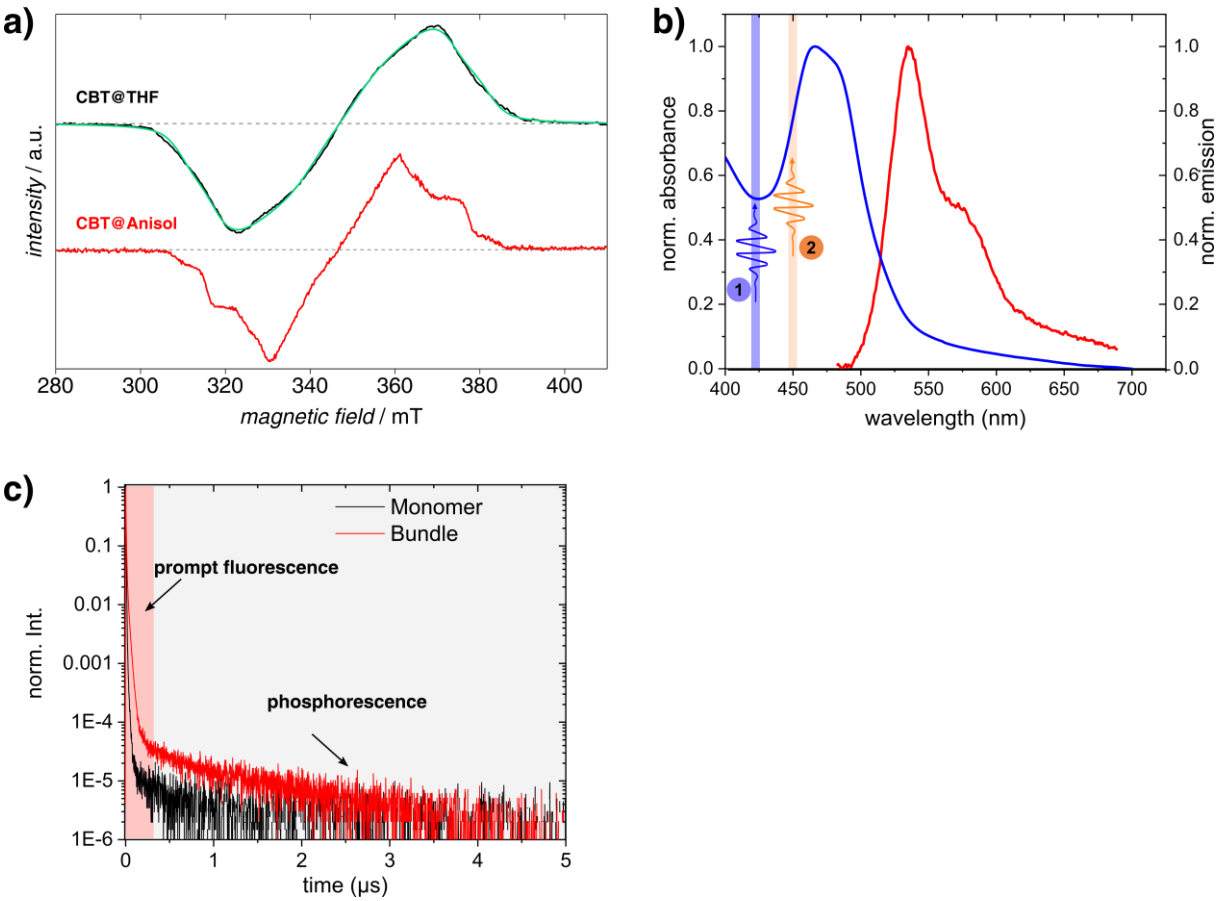


**Fig. S2: TrEPR spectra and photoluminescence decays. a)** TrEPR spectra of a 40 µM dispersion of molecularly dissolved CBT (black) in THF measured at $t = 900\,ns$ after laser excitation of CBT, together with the simulated curve (green) and a 400 µM dispersion of bundles of nanofibres in anisole measured at t = 1300 ns after laser excitation of CBT (red). The parameters used for the simulations are shown in Tab. S1. **b)** Normalized absorption (blue) and fluorescence (red) spectra of bundles of nanofibers in anisole (200 µM)[2]. The spectral positions of the singlet and triplet laser excitation are highlighted in orange and blue respectively (see also Fig. 1 of the main text). **c)** Time-resolved photoluminescence decay of a 40 µM dispersion of molecularly dissolved CBT in THF (black), respectively of a 400 µM dispersion of bundles of nanofibres in anisole (red). Both show a prompt fluorescence signal within nanoseconds and a weaker phosphorescence signal on microsecond time scales. For molecularly dissolved CBT the triplet lifetime is 700 ns (black line), while for the bundles we find a longer lifetime of 1320 ns (red line).

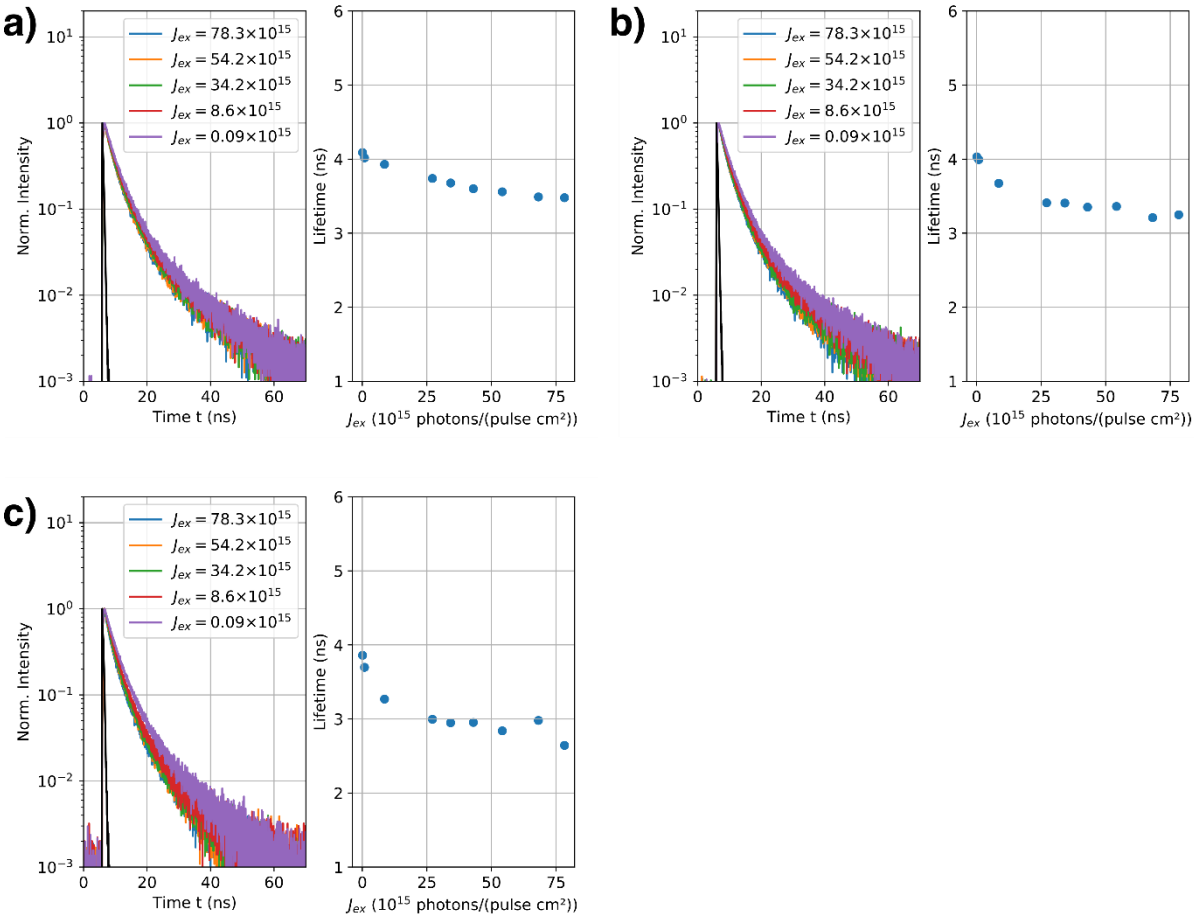


**Fig. S3: Fluorescence decay traces of bundles of nanofibres dispersed in anisole (400 µM) at different excitation fluences.** The laser repetition rates were 0.25 MHz (a), 2.5 MHz (b) and 10 MHz (c). Left parts: Representative fluorescence decay traces for the fluences indicated in the legend in units of photons/(pulse·cm²). The corresponding instrument response functions are shown in black. Right parts: Amplitude-averaged lifetimes of the fluorescence decays as a function of the corresponding fluence. We fitted the data to a convolution of the instrument response function and a bi-exponential fluorescence decay with time constants $t_i$ and relative amplitudes $F_i$. The shown amplitude-averaged lifetimes are calculated according to $t_{av} = \frac{\sum F_i t_i}{\sum F_i}$. Examples of fits are shown in Fig. S4.

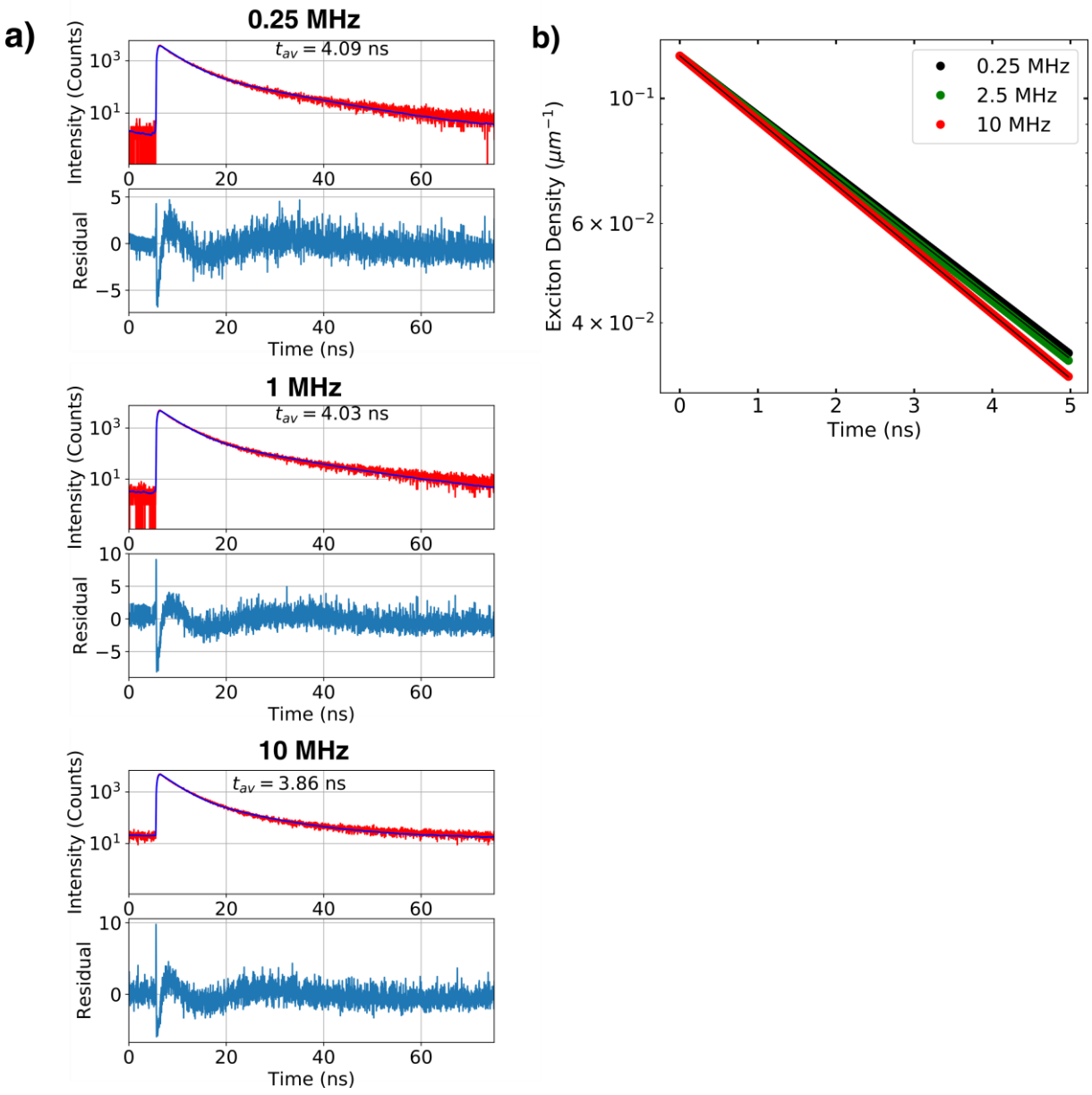


**Fig. S4: Determination of the singlet-triplet annihilation rate in bundles of nanofibres in a 400µM anisole dispersion**. a) Each panel shows, for a fixed excitation fluence of $0.09x10^{15}\ photons/(pulse\ cm^2)$ but different laser repetition rate, a fluorescence decay trace (top, red line) with the corresponding bi-exponential fit function (top, blue line) and the weighted residuals (bottom). For 0.25 MHz we found time constants $t_i$ (relative amplitudes $F_i$) of $t_1 = 3.19\,ns$ $(F_1 = 4174.1)$ and $t_2 = 12.55\,ns$ $(F_2 = 442.92)$. For 2.5 MHz we found $t_1 = 3.18\,ns$ $(F_1 = 5310.06)$ and $t_2 = 12.73\,ns$ $(F_2 = 519.36)$. For 10 MHz we found $t_1 = 3.00\,ns$ $(F_1 = 5188.49)$ and $t_2 = 10.8998\,ns$ $(F_2 = 632.041)$. **b)** To extract the singlet-triplet annihilation rate, we use a simple exponential fit $S_{450}(t) = S_{450}(t=0)e^{(-k+\gamma T_{450})t}$ [7]. Here, $S_{450}(t=0)$ is the total density of the generated singlet excitons at time $t = 0$ after 'singlet laser' excitation at

450 nm, $k$ is the total decay rate for the singlet excitons (without annihilation processes), $\gamma$ is the rate constant of singlet-triplet annihilation and $T_{450}$ is the stationary triplet exciton density formed after intersystem crossing. The singlet exciton density per unit distance of ananofibre in a bundle is estimated according to [8]

$$S_{450}(t=0) = \left(\frac{\chi\lambda_{ex}\left(1-10^{-OD_{ex}}\right)}{hC}\right)\left(\frac{OD_{max}\pi R_b^2}{\epsilon_{max}}\right)^{-1} * a_0^{-1},$$

where $\chi = 6\,x\,10^{-14}J$ is the pulse energy, $R_b = 225nm$ is the radius of excitation, $OD_{exc} = 1.48$ is the optical density of the dispersion at the laser excitation, respectively $OD_{max} = 1.8$ at the absorption maximum, $\lambda_{ex} = 450nm$ is the wavelength of excitation, *hC* is Planck's constant times the speed of light, $\epsilon_{max} = 4500\ (M^{-1}cm^{-1})$ the molar absorptivity at the absorption maximum, and $a_0 = 0.33nm$ is the distance between the monomers along a nanofibre [2]. The product of the first term (number of excitations) and the second term (focal concentration) is a measure for the excitation probability of one monomer within the excitation spot [8]. $T_{450}$ is given by

$$T_{450} = \frac{-k+\sqrt{k^2+4\gamma k_{ISC}S_{450}(t=0)/k_T\tau_{rep}}}{2\,\gamma}.$$

Here, $k_{ICS} = \frac{1}{4.19ns} = 0.238\frac{1}{ns}$ is the intersystem crossing rate, $\tau_{rep}$ is the repetition time of the laser excitation and $k_T = \frac{1}{1320ns}$ is the decay rate for triplet excitons. $k_{ICS}$ is an upper limit, since we assumed that the entire non-radiative channel for singlet exciton decay contributes to intersystem crossing. The fluorescence quantum yield of bundles is $QY = 2.6\%$ [2].

The data shown in (a) are, for simplicity, approximated mono-exponentially, where the decay time corresponds to the amplitude-averaged lifetimes $t_{av} = \frac{\sum F_i t_i}{\sum F_i}$ of our bi-exponential fits. We used a global fit of $S_{450}(t) = S_{450}(t=0)e^{(-k+\gamma T_{450})t}$ to this approximated data set (see b), i.e., this equation is fitted simultaneously to all three traces to obtain the best overall fit. This best fit yields an annihilation rate of

$\gamma = \frac{\mu m}{(80\pm1)ns} = (0.0125 \pm 0.0002)\mu m\, ns^{-1}$.

Since the real intersystem crossing rate is unknown, we also fitted the data to the intersystem crossing rates of $k_{ISC} = 0.0238 \frac{1}{ns}$ ($k_{ISC} = 0.00238 \frac{1}{ns}$), yielding $\gamma = 0.125\ \mu m\ ns^{-1}$ ($\gamma = 1.25\ \mu m\ ns^{-1}$). These additional numbers were then also used for the simulations of the singlet exciton dynamics (see 2. Numerical Simulations).

## 2. Numerical Simulations

The singlet exciton dynamics in the presence of a triplet barrier is simulated by 3 coupled equations. We distinguish between the singlet $S_i$ and triplet population $T_i$ generated by two lasers, indicated by the index $i = 450, 420$ for the 'singlet' 450 nm laser and the 'triplet' 420 nm laser, respectively. These populations relate to one single fibre in the bundle and are given in the unit $\frac{1}{\mu m}$. Note that one bundle comprises more than 1000 nanofibres, yet there is no energy transfer between fibres in bundles[2].

1. $\frac{\partial S_{450(x,t)}}{\partial t} = D_S(t)\frac{\partial^2}{\partial x^2}S_{450}(x,t) - \gamma S_{450}(x,t)T_{450}(x) - kS_{450}(x,t) - \gamma S_{450}(x,t)T_{420}(x)$
2. $\frac{\partial T_{450}(x,t)}{\partial t} \approx 0$
3. $\frac{\partial T420(x,t)}{\partial t} \approx 0$

Here, $D_S$ is the diffusivity of the singlet excitons, $\gamma$ is the singlet-triplet annihilation rate along a fibre in the bundle (Fig. S4) and $k$ is the total decay rate of the bundle's singlet exciton density (in the absence of annihilation). The singlet exciton density generated by the 'triplet' 420 nm laser is not considered here because our experimental conditions ensure that it has already decayed when the 'singlet' laser arrives on the sample. The term $kS_{450}(x,t)$ reflects the (non-)radiative decay of the singlet excitons and does not play a role after normalizing the signal at each point in time for the spatio-temporal maps, analogous to the experiment (Fig. 3b,c). Therefore, this term is no longer considered. During the singlet exciton lifetime, we assume a constant triplet exciton density given by $T_{450,420} = \frac{-k+\sqrt{k^2+4\gamma k_{ISC}S_{450,420}(t=0)/k_T\tau_{rep}}}{2\,\gamma}$, where $S_{450,420}(t=0)$ is the initially generated singlet exciton population by the 'singlet' and the 'triplet' laser, respectively (see Fig. S4). Equation (1.) indicates that singlet-triplet annihilation already occurs for the 'singlet laser' alone. In general, annihilation leads to an additional broadening of the spatio-temporal intensity map. However, this term is not relevant for the changed singlet exciton dynamics in Fig. 3c, since both reference experiment (only 'singlet laser' activated, Fig. 3b) and the experiment with both lasers activated (Fig. 3c) are equally affected by this term. Thus equation (1.) can be simplified to:

4. $\frac{\partial S_{450}(x,t)}{\partial t} \approx D_S(t)\frac{\partial^2}{\partial x^2}S_{450}(x,t) - \gamma T_{420}(x)S_{450}(x,t).$

Hence, the changed singlet exciton dynamics in the presence of triplet excitons can be understood by a simple diffusion equation with an effective singlet-triplet annihilation rate defined as $\gamma_{eff}(x) = \gamma T_{420}(x)$. Equation (4.) is numerically solved using a home written python script to calculate the spatio-temporal fluorescence intensity distributions in Fig. S5 and S6 below.

To reproduce the experimental data, we used the above-estimated parameter set of $= 0.0125\ \mu m\ ns^{-1}$ , $k_{ICS} = \frac{1}{4.19ns}$, $k_T = \frac{1}{1320ns}$ , $k = \frac{1}{4.09\ ns}$ and $\tau_{rep} = 200\ ns$ (see Fig. S4 and Tab. S2). Without loss of generality, we choose $D_S = 0.1\frac{cm^2}{s}$ in accordance with our previous work [2]. Assuming uniform intensities within the Gaussian laser foci of the singlet and triplet laser, we have estimated the initial exciton populations. The absorption cross section of $\sigma_{450nm} = 1.4\text{x}10^{-17}\text{cm}^2$ and the excitation intensity of 115 W cm$^{-2}$ for the singlet laser leads to approximately 0.5 absorbed photons per pulse within the Gaussian excitation spot along one fibre in a bundle, i.e., $S_{450}(t=0) \approx \frac{0.5}{211\ nm} \approx 2\ \mu m^{-1}$. The absorption cross section of $\sigma_{420nm} = 1.03\text{x}10^{-17}\text{cm}^2$ and the excitation intensity of 540 W cm$^{-2}$ for the triplet laser leads to the generation of approximately 2 singlet excitons per pulse within the Gaussian excitation spot along one fibre in a bundle, i.e., $S_{420}(t=0) \approx \frac{2}{265\ nm} \approx 7.5\mu m^{-1}$. These singlets can diffuse, radiatively decay or can be converted to triplets by intersystem crossing. The fact that the singlets can move beyond the excitation spot of the triplet laser via diffusion prior to intersystem crossing results in a broadened distribution for the triplets. We calculate the width of this new distribution by solving the following differential equation for the triplet laser exciton densities in the absence of the singlet laser (see Fig. S5b).

5. $\frac{\partial S_{420(x,t)}}{\partial t} = D_S(t)\frac{\partial^2}{\partial x^2}S_{420}(x,t) - \gamma S_{420}(x,t)T_{420}(x,t) - kS_{420}(x,t)$
6. $\frac{\partial T_{420}(x,t)}{\partial t} \approx k_{ICS}S_{420}(x,t) - k_T T_{420}(x,t)$

Starting from a Gaussian singlet distribution with a FWHM of 265 nm, we obtain a Gaussian triplet population with a FWHM of 560 nm at $t = 120\ ns$ (Fig. S5b top). Because the singlet decays within its lifetime and we assume the triplet to be immobile, the triplet distribution does not broaden with time for $t > 20\ ns$.

Due to the repeated laser excitation, we assume a quasi-static triplet density corresponding to $T_{420} = \frac{-k+\sqrt{k^2+4\gamma k_{ISC} S_{420}(t=0)/k_T \tau_{rep}}}{2\,\gamma} \approx 23\ \mu m^{-1} \approx \frac{13}{560\ nm}$ . For our setting, we thus generate 13 triplets per nanofibre randomly distributed within our triplet laser excitation, where they can act as a local barrier. The used parameters are summarized in Tab. S2.

For the spatial distribution of both the singlet and the triplet exciton population, we assume Gaussian initial distributions with standard deviations according to the experimental conditions (see Fig. S10), i.e., the integral over these Gaussian distributions gives the above-mentioned number of singlet and triplet excitations respectively.

Using the parameters estimated above for our CBT-based bundles of nanofibres we show in Fig. S5c the simulated spatio-temporal singlet exciton dynamics without (top) and with a triplet population (bottom) for a (centre-of-mass) distance of 800 nm between the populations. Those simulations reproduce the situation in Fig. 3 of the main text including the reduction in diffusion length $\Delta L_D$ very well.

To demonstrate that our approach is not limited to the very specific set of photophysical parameters of our bundles, we present in Fig. S6 a series of simulations, where we systematically varied the distance between the lasers (= centre-of-mass distance between initial populations), the annihilation rate $\gamma$ and the triplet density $T_{420}$.

The annihilation rate $\gamma$ depends on two system specific quantities[9]:

- the exciton capture radius, i.e., the maximum distance between singlet and triplet excitons to allow for annihilation, which typically does not exceed a few molecules and thus does not change much for different systems;
- the diffusion constants of singlet excitons, which varies for different supramolecular nanostructures (note that the triplet exciton diffusion constant is typically orders of magnitude smaller than that of singlet excitons, and within the singlet exciton lifetime triplet excitons are therefore quasi-static).

The triplet density $T_{420}$.depends on:

- the intersystem crossing rate both from the excited singlet into the triplet state as well as from the triplet state into the singlet ground state; those rates are

system-specific and be enhanced e.g. by using supramolecular building blocks with greater spin-orbit coupling induced by, e.g., heavy metal atoms;

- the density of the initial singlet population prior to intersystem crossing, which can be controlled by the power of the 'triplet laser' over a wide range (and the pulse repetition rate to some extent, only photobleaching is the limiting factor here).

We note again that in the diffusion equation for singlet excitons in the presence of a triplet population [Eq. (4)] only the product $\gamma T_{420} = \gamma_{eff}$, i.e., an effective annihilation rate, is important. In other words, the triplet density $T_{420}$ can be chosen, by an appropriate choice of the power of the 'triplet laser', such that effective annihilation rate is tuned to a regime where the triplet gate displays the desired effect, independent of the actual (system-specific) photophysical parameters.

In Fig. S6 we have shown the spatio-temporal singlet exciton dynamics in the presence of the triplet population as a function of this effective rate varied over two orders of magnitude. While Fig. S6b (left) re-displays Fig. S5c (bottom), i.e., the situation in our experiments with 800 nm between the lasers and $\gamma_{eff} = 0.29\, ns^{-1}$(with $\gamma = 0.0125 \frac{\mu m}{ns}$ and $T_{420} = 23 \frac{1}{\mu m}$) Fig. S6a and c show simulations with $\gamma_{eff} = 0.029\, ns^{-1}$ and $\gamma_{eff} = 2.9\, ns^{-1}$ , respectively. We find that $\Delta L_D$ increases from 2 nm to 19 nm and finally to 53 nm from panels a to c.

In contrast, using $\gamma_{eff} = 0.29\, ns^{-1}$ for our system and reducing the distance between the singlet and triplet populations from 800 to 400 nm, we find only an increase in $\Delta L_D$ from 19 nm to 28 nm (Fig. S6b). Already at a (centre-of-mass) distance of 800 nm there is a substantial overlap between the populations (Fig. S6b). Therefore, compared to enhancing $\gamma_{eff}$, the effect of reducing the distance between the populations is less pronounced.

We note that also the simulation of the full equation (1.) leads to similar results. Finally a direct excitation from the singlet ground state to the first excited triplet state is in principle possible but requires high laser power due to the typically very small absorption cross-sections for this transition.

**Table S2. Parameters for the simulation of the tailored spatio-temporal singlet-triplet annihilation** shown in Fig. S5. For details see section 2.

| $S_{450}$ | $T_{420}$ | $k$ | $k_{ICS}$ | $k_T$ | $\tau_{rep}$ | $\gamma$ | $D_S$ |
|---|---|---|---|---|---|---|---|
| $2\,\frac{1}{\mu m}$ | $23\,\frac{1}{\mu m}$ | $\frac{1}{4.09\,ns}$ | $\frac{1}{4.19 ns}$ | $\frac{1}{1320 ns}$ | $200\,ns$ | $0.0125\,\frac{\mu m}{ns}$ | $0.1\,\frac{cm^2}{s}$ |

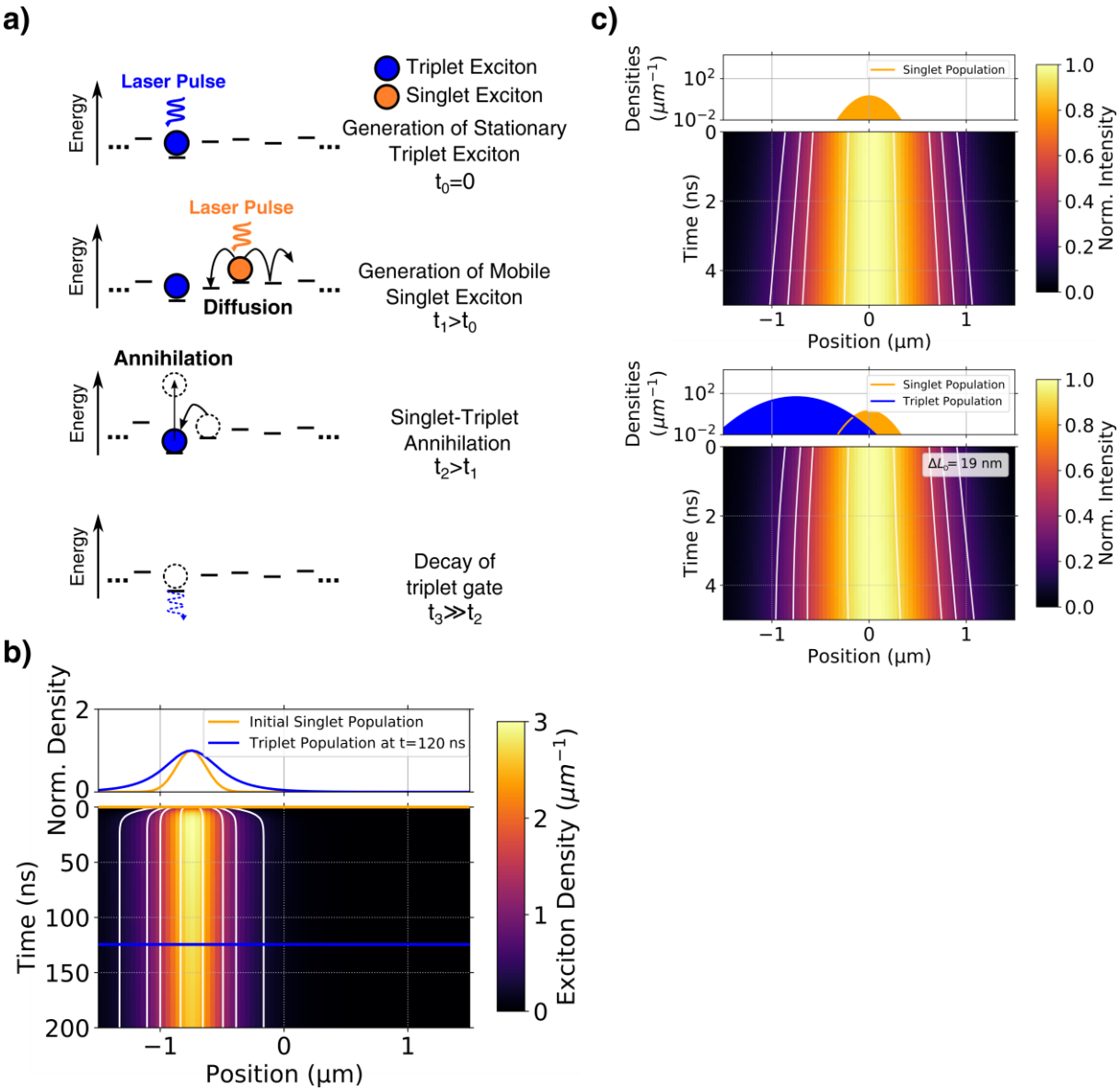


**Fig. S5: Schematic illustration and numeric simulation of tailored spatio-temporal singlet-triplet annihilation. (a)** Schematic illustration of gated singlet exciton diffusion: At $t_0 = 0$ a laser pulse creates an initial singlet exciton that is converted into a triplet exciton (blue filled circle) via intersystem crossing. A second laser arriving at $t_1 > t_0$ creates mobile singlet excitons (orange filled circle), spatially separated from the triplet population. At $t_2 > t_1$, the mobile singlet exciton encounters the triplet exciton and annihilation takes place, leaving behind only a triplet exciton (self-sustaining barrier, see main text). Finally, at time $t_3 >> t_2$ the triplet exciton decays (by phosphorescence or non-radiatively) and the gate is deactivated. **b)** Simulated triplet exciton dynamics generated by the triplet laser excitation in the absence of the singlet laser. The initial Gaussian singlet density (orange, top panel) is transformed into a broader triplet population (blue, top panel) due to diffusing singlets

prior to intersystem crossing. **c)** Simulated singlet exciton diffusion in the absence (top) and the presence of a triplet population (below) at a distance of -800 nm to the left of the singlet population. For details see section 2. Numerical Simulations and for the used simulation parameters Tab. S2.

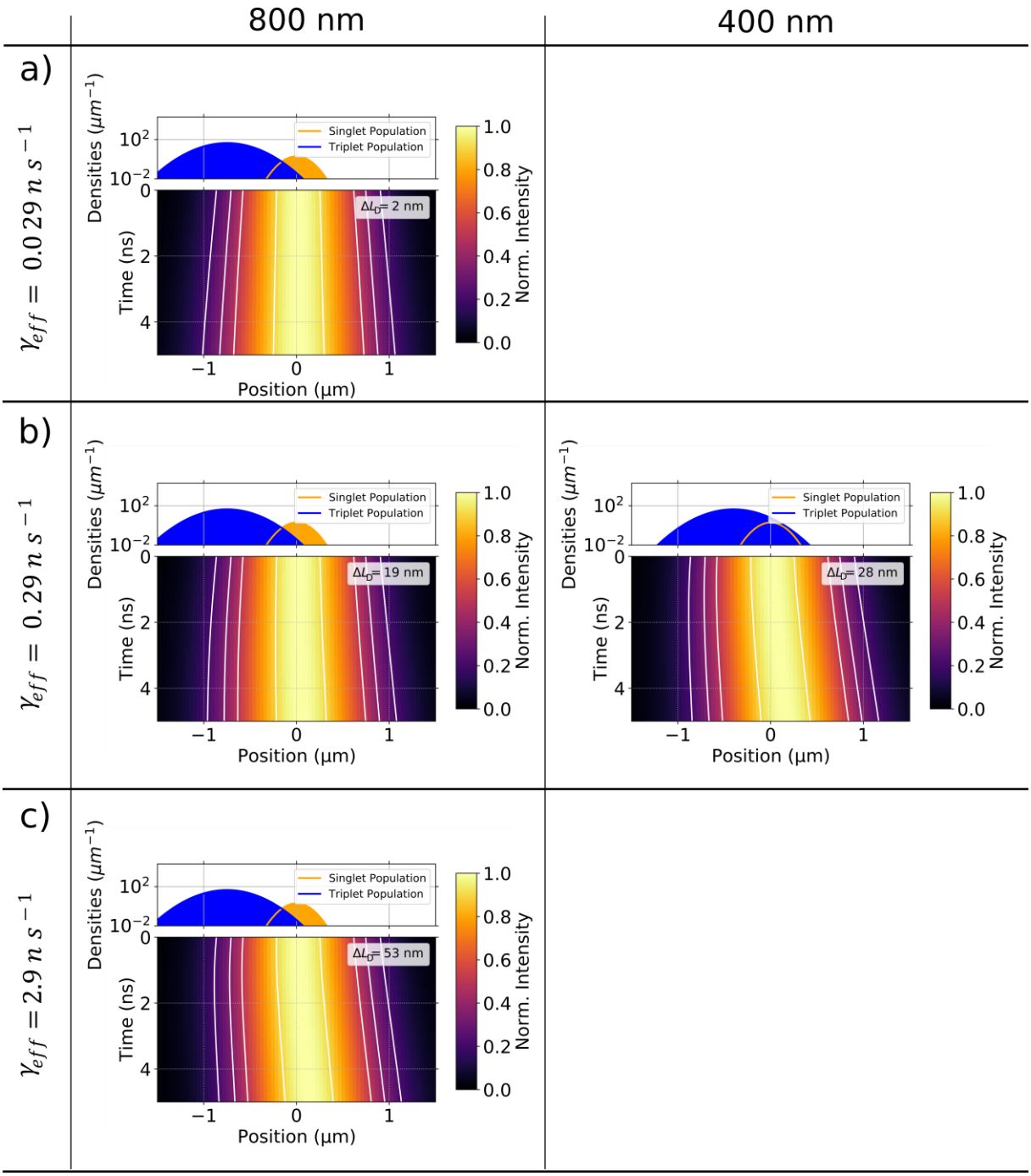


**Fig. S6: Parameter study of tailored spatio-temporal singlet-triplet annihilation**. From panel a to c, the effective annihilation rate $\gamma_{eff}$ increases, while the distance between singlet and triplet population is kept constant (-800 nm). In panel b (right) this distance is reduced to 400 nm. The simulation parameters can be found in Section 2 and in table S2. The changed parameters are indicated in the corresponding illustration. For more detail, see Section 2.

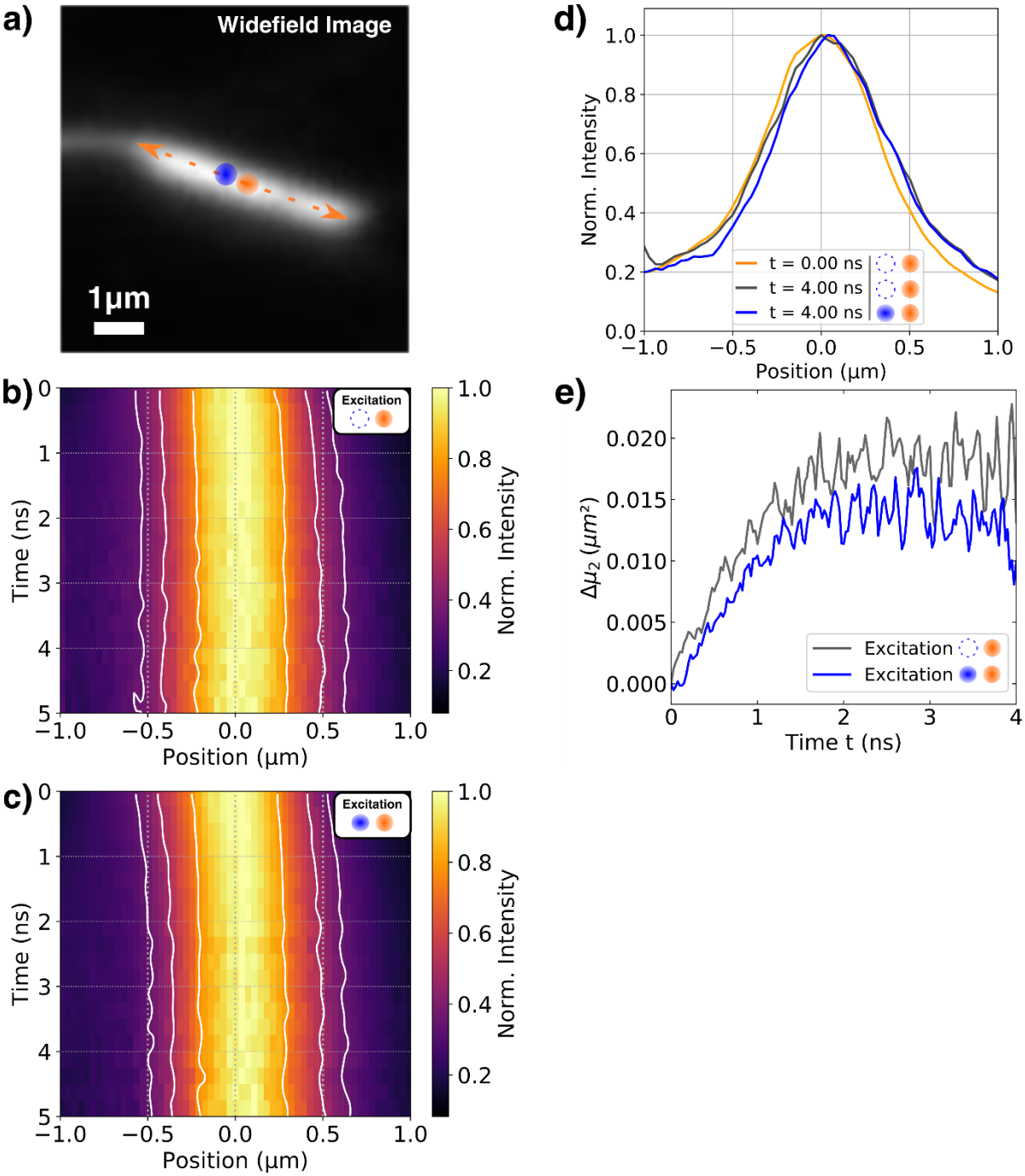


**Fig. S7: Direct visualization of controlled singlet exciton transport in another single bundle of supramolecular nanofibres. a)** Widefield image of an individual bundle. Orange dashed arrows indicate the detection scanning axis $x$. The orange circle labels the position $x = 0$ of the singlet population. The blue circle indicates the position of the triplet population at $x \approx -500nm$. **b)** Normalized fluorescence intensity distributions and its evolution in space and time for the bundle in (a) for the measurement with only the 'singlet laser' activated. The asymmetric broadening indicates bleaching at the position of the 'triplet laser' (on the left side, $x < 0\mu m$) **c)**

Normalized fluorescence intensity distribution as in (b), but here both the ‘singlet’ and ‘triplet laser’ are activated. The triplet population is generated on the left side of the map. Due to the small distance between the two lasers, the entire singlet population seems to “move” away from the position of the triplet laser. The white contour lines in (b,c) indicate the widths of the intensity profiles. **d)** Intensity profiles retrieved from the fluorescence intensity maps in b) (grey) and c) (blue) at different delay times $t$ after singlet exciton generation. The orange line shows the initial intensity distribution at time $t = 0$ generated by the ‘singlet laser’. For the reference experiment, we can detect only a small broadening of the profiles for positions x < 0 µm due to photobleaching, while for the other direction, the broadening is clearly evident (x > 0 µm, compare orange and grey lines).

For the experiment with both lasers activated, the profile at $t = 4ns$ (blue line) clearly shows a reduced intensity for positions x<0 µm compared to the initial profile at $t = 0$ (orange line). To the right (x > 0 µm) singlet exciton diffusion is entirely unperturbed since the profiles in the absence (grey line) and presence (blue line) of the triplet population overlap. **e)** Temporal changes of the second moments $\Delta\mu_2$ (widths) of the spatial intensity profiles determined from the data in (b) (grey) and (c) (blue).

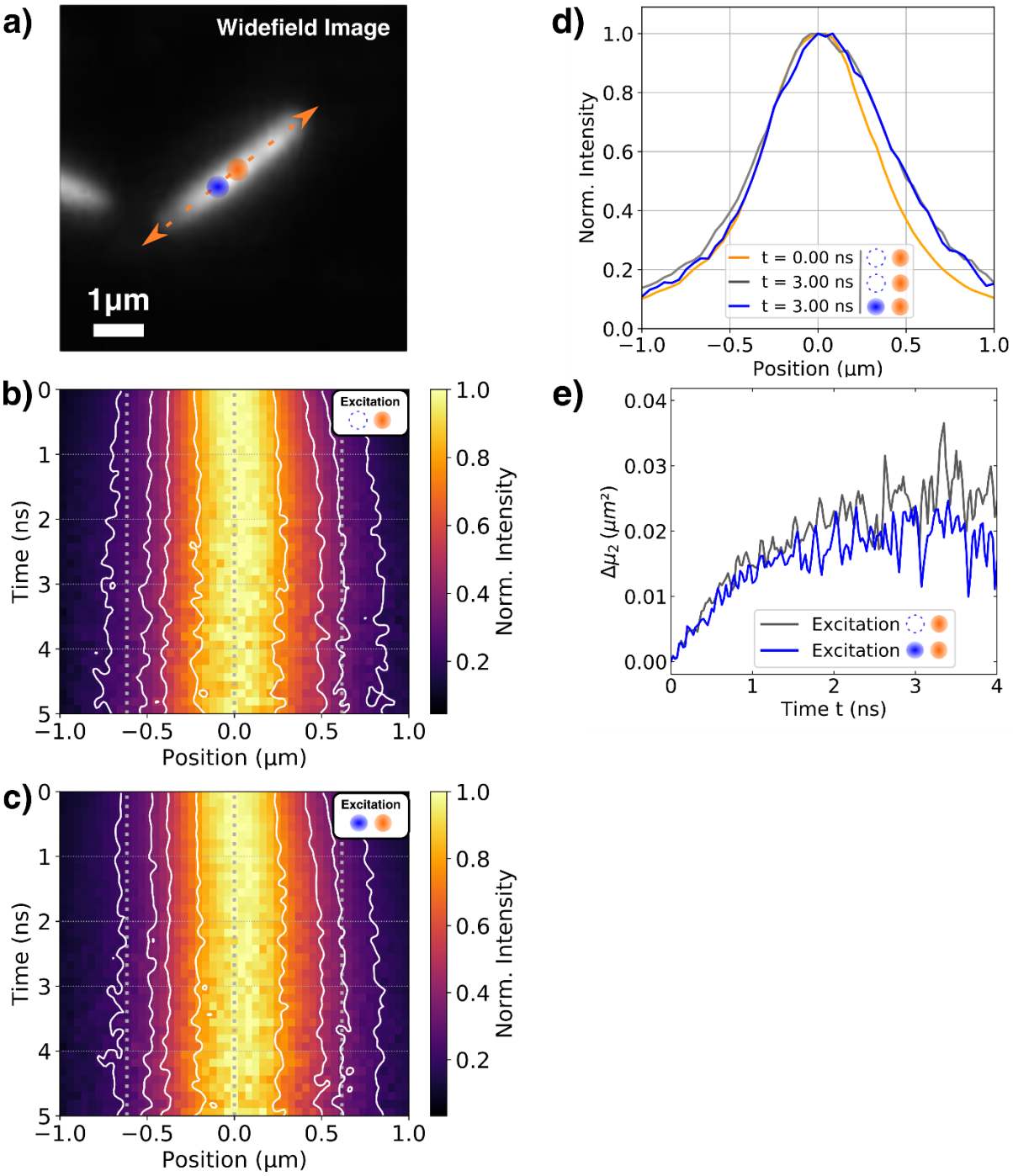


**Fig. S8: Direct visualization of controlled singlet exciton transport in another single bundle of supramolecular nanofibres. a)** Widefield image of an individual bundle. Orange dashed arrows indicate the detection scanning axis $x$. The orange circle labels the position $x = 0$ of the singlet population. The blue circle indicates the position of the triplet population at the position $x \approx -600\,nm$. **b)** Normalized fluorescence intensity distributions and its evolution in space and time for the bundle in (a) for the measurement with only the 'singlet laser' activated. **c)** Normalized fluorescence intensity distribution as in (b), but here both the 'singlet' and 'triplet laser'

are activated. The triplet population is generated on the left side of the map. The white contour lines in (b,c) indicate the widths of the intensity profiles. **d)** Intensity profiles retrieved from the fluorescence intensity maps in b) (grey) and c) (blue) at different delay times $t$ after singlet exciton generation. The orange line shows the initial intensity distribution at time $t = 0$ generated by the 'singlet laser'. While for positions x < 0 µm the initial (orange line) and delayed (blue line) profiles partly overlap, i.e., spatial broadening of the initial singlet exciton population is hindered, to the right (x > 0 µm) singlet exciton diffusion is entirely unperturbed since the profiles in the absence (grey line) and presence (blue line) of the triplet population overlap. **e)** Temporal changes of the second moments $\Delta\mu_2$ (widths) of the spatial intensity profiles determined from the data in (b) (grey) and (c) (blue).

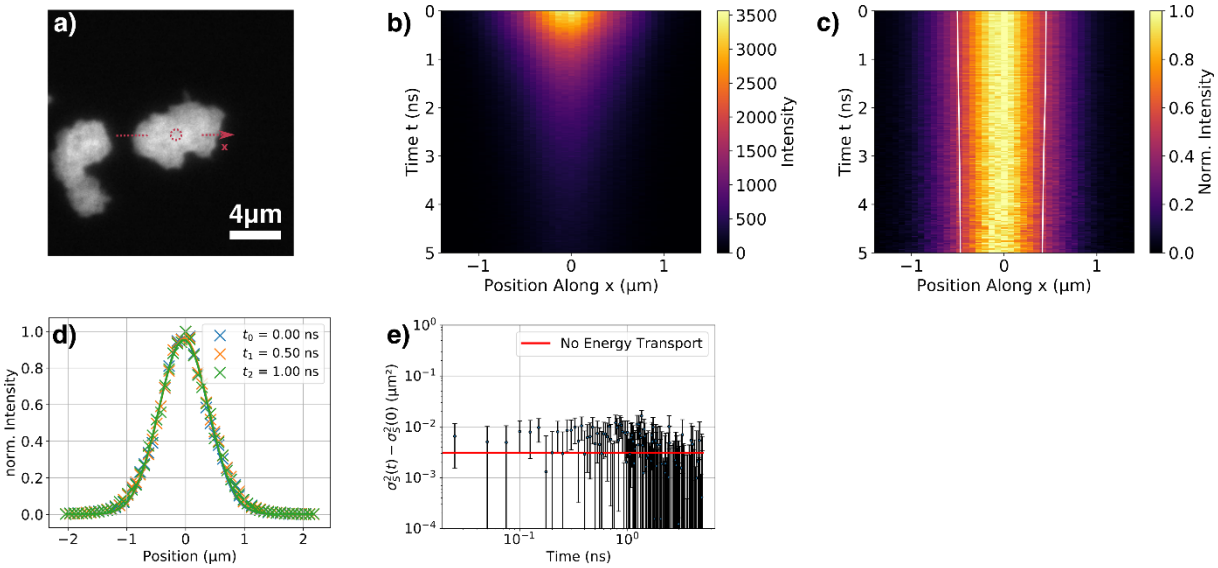


**Fig S9: Control experiment. a)** Widefield PL image of agglomerated SiOx-nanobeads. The dashed red circle and arrow illustrate the position of confocal excitation and the direction of the detection scanning (x-axis), respectively. b**)** Spatio-temporal PL intensity distribution $I(x,t)$. **c)** Normalized PL intensity distribution as it evolves in space and time, measured along the axis illustrated by the red dashed arrow in A). The position x denotes the distance relative to the excitation position (x=0) along the arrow in A), and t = 0 ns corresponds to the arrival time of the excitation pulse. To emphasize changes in the width of the distribution, it is normalized at each time step. The contour lines indicate the time evolution of the full width at half maximum. d**)** Illustration of the normalized spatial intensity distribution $I(x,t_i)$ for three times $t_i$ and the corresponding Gaussian fits, yielding e.g. a standard deviation of $\sigma_I\,(t=0) = 411\,nm$. Note that this number is determined by the convolution of the Gaussian excitation profile, the detection point-spread function and the detector chip size. **e)** Temporal changes of the second moments of the singlet excitons, revealing no resolvable energy transport in agglomerated SiOx-nanobeads. Taken from Ref. [2].

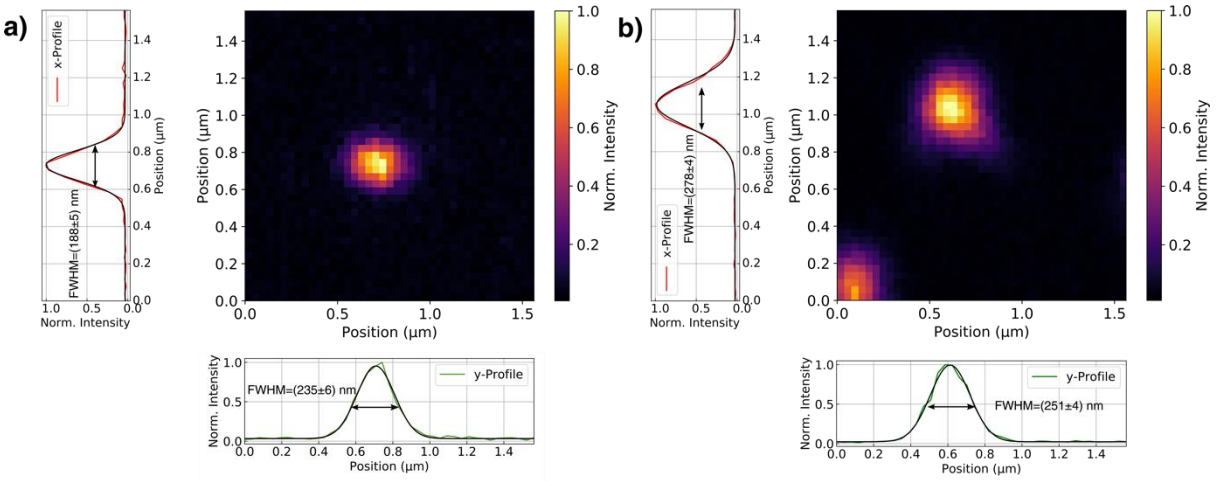


**Fig S10: Characterisation of the laser foci.** a) 450 nm 'singlet' laser. b) 420 nm 'triplet' laser. We raster scanned single fluorescence microspheres (0.1µm diameter, Red Fluorescence Carboxylated Ps Latex, Nanosphere) along the laser excitation spot to characterise their sizes. The confocal image is shown as a map with colour-coded intensity. The shown profiles are along the x- and y-scanning axis and were placed through the intensity maximum of the map.

## 2. References


1 A. T. Haedler, S. C. J. Meskers, R. H. Zha, M. Kivala, H. W. Schmidt and E. W. Meijer, *J. Am. Chem. Soc.*, 2016, **138**, 10539–10545.

2 B. Wittmann, F. A. Wenzel, S. Wiesneth, A. T. Haedler, M. Drechsler, K. Kreger, J. Köhler, E. W. Meijer, H.-W. Schmidt and R. Hildner, *J. Am. Chem. Soc.*, 2020, **142**, 8323–8330.

3 A. T. Haedler, K. Kreger, A. Issac, B. Wittmann, M. Kivala, N. Hammer, J. Köhler, H.-W. Schmidt and R. Hildner, *Nature*, 2015, **523**, 196–199.

4 T. Biskup, *Front. Chem.*, 2019, **7**, 10.

5 D. L. Meyer, F. Lombeck, S. Huettner, M. Sommer and T. Biskup, *J. Phys. Chem. Lett.*, 2017, **8**, 1677–1682.

6 S. Stoll and A. Schweiger, *J. Magn. Reson.*, 2006, **178**, 42–55.

7 Y. Zaushitsyn, K. G. Jespersen, L. Valkunas, V. Sundström and A. Yartsev, *Phys. Rev. B*, 2007, **75**, 195201.

8 J. R. Caram, S. Doria, D. M. Eisele, F. S. Freyria, T. S. Sinclair, P. Rebentrost, S. Lloyd and M. G. Bawendi, *Nano Lett.*, 2016, **16**, 6808–6815.

9 A. Köhler and H. Bässler, *Electronic processes in organic semiconductors: An introduction*, Wiley-VCH Verlag GmbH & Co. KGaA, Weinheim, Germany, 2015.